ACS NANO

www.acsnano.org

ARTICLE

Supersaturated Doping-Induced Maximized Metal–Support Interaction for Highly Active and Durable Oxygen Evolution

Hanwen Liu, Wenhui Shi, Yaqing Guo, Yunjie Mei, Yi Rao, Jinli Chen, Shijing Liu, Cheng Lin, Anmin Nie, Qi Wang, Yifei Yuan, Bao Yu Xia,* and Yonggang Yao*

Cite This: https://doi.org/10.1021/acsnano.4c09249

ABSTRACT: Metal–support interaction (MSI) is pivotal and ubiquitously used in the development of next-generation catalysts, offering a pathway to enhance both catalytic activity and stability. However, owing to the lattice mismatch and poor solubility, traditional catalysts often exhibit a metal-on-support heterogeneous structure with limited interfaces and interaction and, consequently, a compromised enhancement of properties. Herein, we report a universal and tunable method for supersaturated doping of transition-metal carbides via strongly nonequilibrium carbothermal shock synthesis, characterized by rapid heating and swift quenching. Our results enable ~20 at. % Ni_2FeCo doping in Mo_2C, significantly surpassing the thermodynamic equilibrium limit of <3 at. %. The supersaturation ensures more catalytically active NiFeCo doping and sufficient interaction with Mo_2C, resulting in the maximized MSI (Max-MSI) effect. The Max-MSI enables outstanding activity and particularly stability in alkaline oxygen evolution reaction, showing an overpotential of 284 mV at 100 mA cm^{-2} and stable for 700 h, while individual Ni_2FeCo and Mo_2C only last less than 70 and 10 h (completely dissolved), respectively. In particular, the SD-Mo_2C catalyst also exhibits excellent durability at 100 mA cm^{-2} for up to 400 h in 7 M KOH. Such a significantly improved stability is attributed to the supersaturated doping that led to each Mo atom strongly binding with adjacent heteroatoms, thus elevating the dissolution potential and corrosion resistance of Mo_2C at a high current density. Additionally, the highly dispersed NiFeCo also facilitates the formation of dense oxyhydroxide coating during reconstruction, further protecting the integrated catalysts for durable operation. Furthermore, the synthesis has been successfully scaled up to fabricate large (16 cm^2) electrodes and is adaptable to nickel foam substrates, indicating promising industrial applications. Our strategy allows the general and versatile production of various highly doped transition-metal carbides, such as Ni_2FeCo-doped TiC, NbC, and W_2C, thus unlocking the potential of maximized or adjustable MSI for diverse catalytic applications.

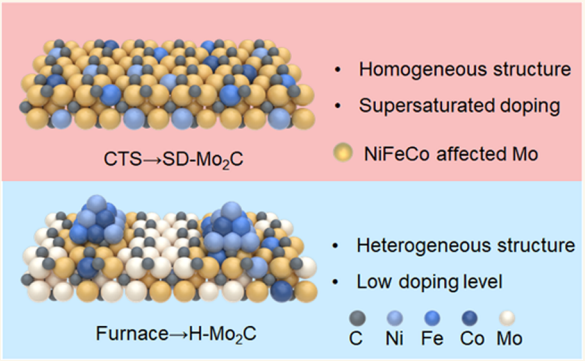

KEYWORDS: *oxygen evolution reaction, carbide catalyst, carbothermal shock, nonequilibrium synthesis, supersaturated doping*

INTRODUCTION

Among the various strategies for harnessing and storing renewable energy, electrolytic water splitting to generate hydrogen stands out as a promising solution.[1,2] However, the efficiency and feasibility of water splitting are heavily dependent on the performance of catalysts used in the oxygen evolution reaction (OER), which often show a high overpotential and rapid performance degradation owing to the harsh catalytic environment.[3,4] Transition-metal-based catalysts have shown good activity and stability for alkaline water electrolysis, during which they in situ reconstructed into hydroxides with a large specific surface area and high activity.[5,6] However, their demonstrated durability is far from satisfactory in practice under highly corrosive OER conditions.[7,8] As such, tremendous ongoing research in this field is focused on developing more efficient and durable OER catalysts to meet the demands of sustainable energy production.[9,10]

Metal–support interaction (MSI) is a critical concept in developing next-generation catalysts and further modulating

Received: July 10, 2024
Revised: October 2, 2024
Accepted: October 7, 2024

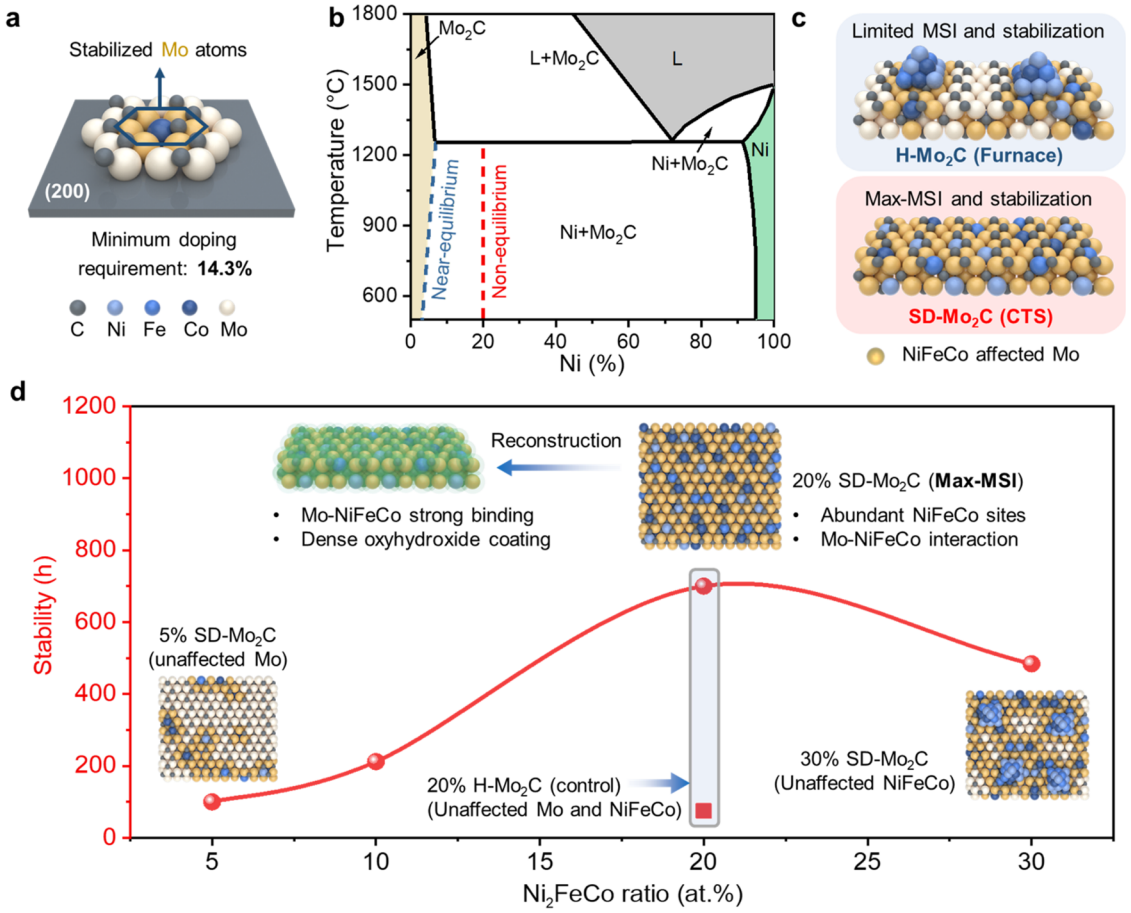

Figure 1. (a) Schematic diagram showing the influence of doped atoms in the Mo_2C. (b) Pseudo-binary phase diagram of Ni−Mo_2C under equilibrium conditions, where the nonequilibrium process increases the solubility of Ni in Mo_2C (red dashed line). (c) Schematic illustration of the homogeneous SD-Mo_2C derived from CTS and the heterogeneous H-Mo_2C synthesized by furnace treatment. (d) Effect of the Ni_2FeCo doping ratio on the OER durability. Inset: schematic illustration of the catalyst structure and MSI, where Max-MSI features mutually interacted Mo and NiFeCo atoms, while other structures have either unaffected Mo or NiFeCo, resulting in less stability under highly corrosive OER.

their performances, which stands as a few strategies that can simultaneously improve the catalytic activity and stability.[11,12] While the metal behaves as the primary catalyst, the support can effectively disperse and stabilize the metal catalyst through strong structural and electronic interactions and synergistic effects at the interfaces, thereby improving the activity and stability.[13−16] Carbides have been widely used as support materials due to their high electrical conductivity.[17,18] For example, Li reported Fe and Ni atoms anchored on the surface of WC_x,[17] which exhibited electronic interactions between metals and W atoms that help stabilize the FeNi atoms. NiFe-WC_x achieved an overpotential of 237 mV and maintained stability after the 1000 h test at 10 mA cm^{-2}. Hou reported Ni single atoms supported on oxygen-incorporated Mo_2C via Ni−O−Mo bonds,[18] showing enhanced catalytic activity via the strong electron coupling between Ni atoms and the Mo_2C carrier. This MSI catalyst exhibits an overpotential of 299 mV at 10 mA cm^{-2} and long-term stability over 16 h. Unfortunately, these catalysts often show a metal-on-top-support heterogeneous structure and have very limited interfaces to induce sufficient MSI for property enhancement. The decorated surfaces are only stable at a low current density (~10 mA cm^{-2}) and become drastically unable at industrially relevant conditions (>100 mA cm^{-2}) because of severe reconstruction and dissolution of both metal and metal carbide at elevated potentials. Therefore, enabling more/supersaturated doping into the support would result in pronounced MSI and activation, enhancing the overall structure stability and making them suitable for the OER at large current densities or high potentials.

The limited interfaces and interactions are mainly attributed to the significant differences between the metal and support structures (e.g. lattice matching), resulting in limited solubility and MSI.[19,20] The solubility limits of metals (Fe, Co, and Ni) in the support (TiO_2, CeO_2, MoS_2, and WC) are usually relatively low and affected by the following temperature: Fe and Co in TiO_2 (4 at. % at 800 °C),[21,22] Ni in MoS_2 (7.5 at. % at 400 °C),[23] and Fe in CeO_2 (3 at. % at 1100 °C).[24] The solubility of metal Co in carbide (WC) is too low to be measured.[25] Notably, oxide supports with naturally poor electronic conductivity would easily lead to increasing overpotentials and ohmic impedance, while more conductive supports, such as carbides,[26] are often extremely hard to dope or manipulate during the catalyst synthesis. Thus, developing heterogeneous catalysts that could largely unlock and maximize the potential of MSI is both intriguing and a significant challenge.[27,28]

In this study, we employ the carbothermal shock (CTS) method, a strongly nonequilibrium synthesis technique that involves rapid heating followed by immediate quenching,[29−34]

https://doi.org/10.1021/acsnano.4c09249
ACS Nano XXXX, XXX, XXX−XXX

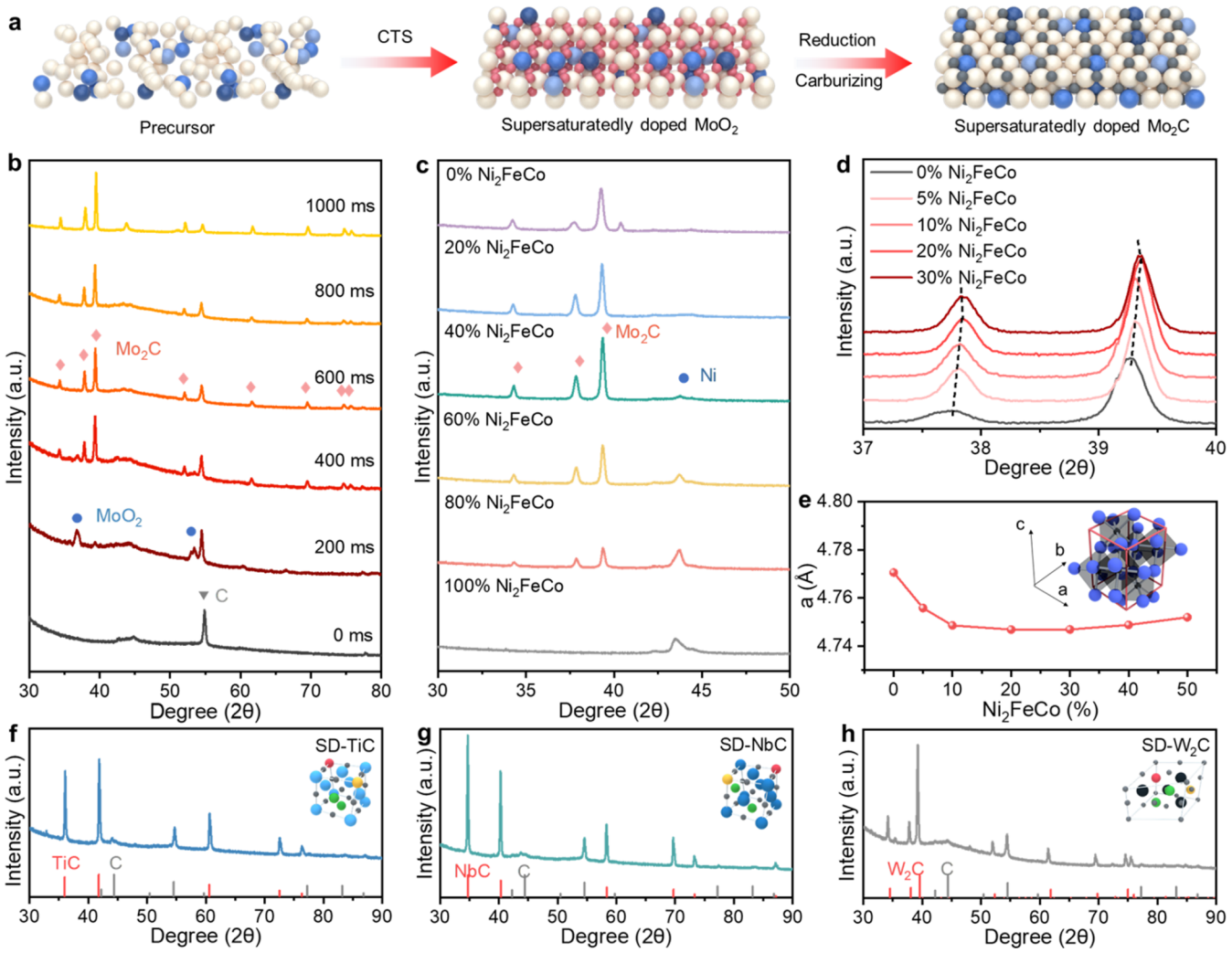

Figure 2. (a) Schematic illustration of the preparation process for the SD-Mo_2C electrocatalyst. (b) XRD patterns of 20% SD-Mo_2C during the synthesis process. (c) XRD patterns of carbides with different Ni_2FeCo ratios (0−100%). Excessive dopant input will lead to the precipitation of the Ni_2FeCo alloy. (d) Variation in diffraction angles of SD-Mo_2C with different Ni_2FeCo ratios (0−30%). (e) Influence of Ni_2FeCo ratio on the lattice parameter a of SD-Mo_2C, with the inset showing a schematic crystal structure of orthorhombic Mo_2C. (f−h) XRD patterns of SD-TiC, SD-NbC, and SD-W_2C.

to synthesize a supersaturated doping Mo_2C (SD-Mo_2C) with approximately 20 at. % of Ni_2FeCo dopants. This level of supersaturation goes beyond the thermodynamic equilibrium and scarce doping of Ni into Mo_2C (~8 at. % at 1250 °C, ~3 at. % at room temperature) and ensures the maximized interaction between Mo_2C and NiFeCo atoms, thereby augmenting the activity and especially improving the durability of the carbides catalyst at high current density in the OER. This pronounced interplay between the metal dopant and the support is characterized as maximized metal support interaction (Max-MSI), which is pivotal for achieving optimal catalytic performance with concurrently high activity and durability.

RESULTS AND DISCUSSION

Material Synthesis and Characterization. To maximize the interaction between the dopant and the support atoms, at least one heteroatom must exist in each cell to activate and particularly stabilize Mo in Mo_2C, which has a dissolution potential lower than that of the respective oxides or oxyhydroxide of NiFeCo. As shown in Figure 1a, each surface Mo atom of orthorhombic Mo_2C is encircled by six neighboring Mo atoms, creating a hexagonal coordination environment. To ensure that each Mo site within the structure can be affected by the adjacent heteroatoms, the minimum doping content of Mo_2C is 14.3 at. % for surface Mo atoms. However, considering the inherent randomness in the doping process, including the variability in content and the specific sites occupied by the dopants, the actual doping content should be higher than 14.3 at. % to ensure comprehensive coverage and interaction over the entire Mo lattice.

To achieve the presence of more heteroatoms in Mo_2C, supersaturation doping is required (Figure 1b) demonstrates the nonequilibrium synthesis strategy of the SD-Mo_2C. According to the pseudo-binary phase diagram of $NiMo_2C$,[35] the maximum doping of Ni in Mo_2C under equilibrium conditions is about 8 at. % at 1250 °C. As the temperature decreases, the second phase of Ni precipitates, leading to a decline doping content of Ni, as indicated by the blue dotted line (<3 at. % at room temperature). On the contrary, the CTS method enables the formation of an SD-Mo_2C due to the nonequilibrium process, represented by the red dotted line. To

https://doi.org/10.1021/acsnano.4c09249
ACS Nano XXXX, XXX, XXX−XXX

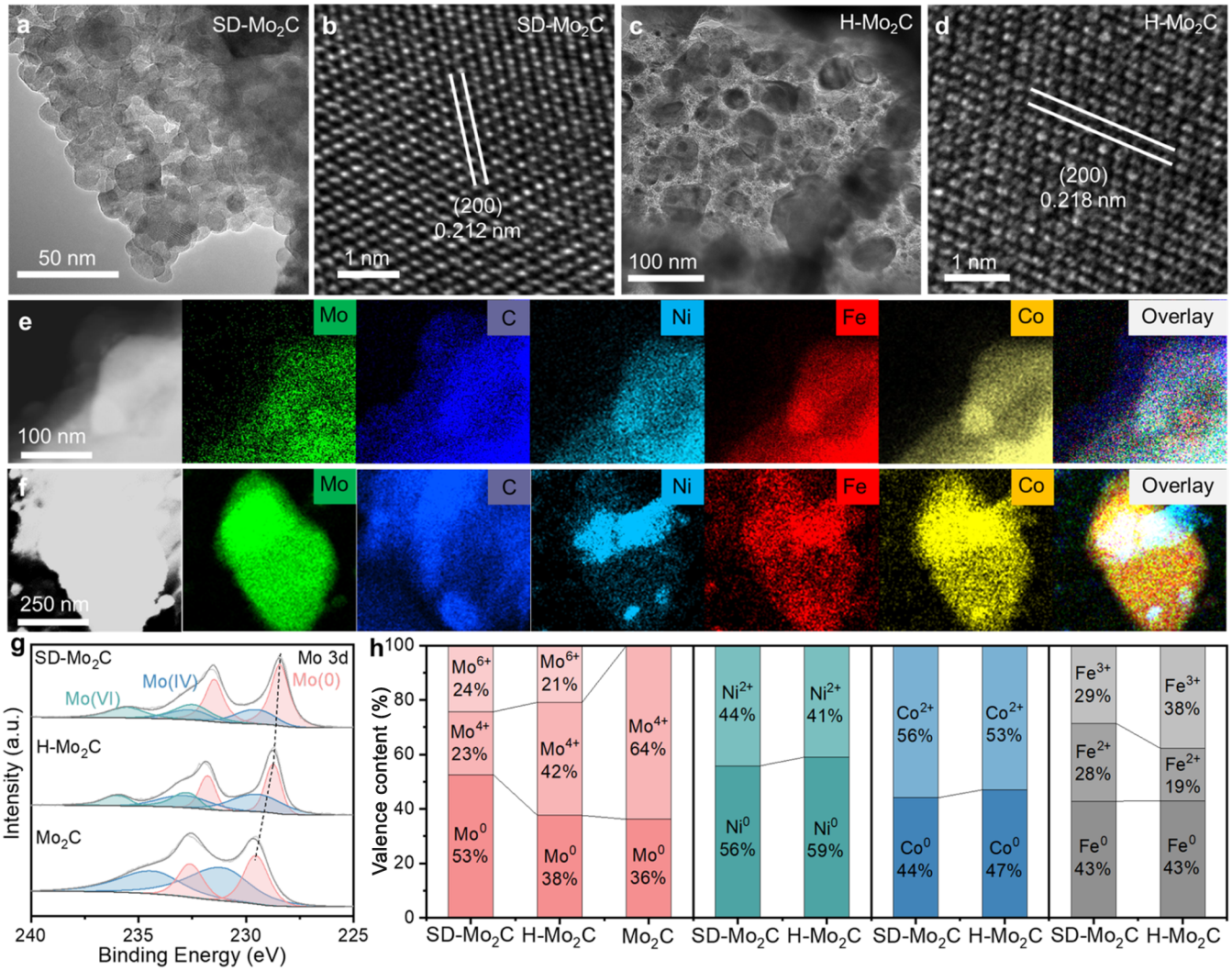

Figure 3. Structural analysis of SD-Mo_2C. (a) TEM image of SD-Mo_2C. (b) HR-TEM image of SD-Mo_2C lattice. (c) TEM image of SD-Mo_2C. (d) HR-TEM images of H-Mo_2C lattice. (e, f) EDX mapping image of SD-Mo_2C and H-Mo_2C. (g) High-resolution Mo 3d X-ray photoelectron spectroscopy (XPS) spectra of SD-Mo_2C, H-Mo_2C, and Mo_2C. (h) Valence distribution of each metal element in the above materials.

verify that the thermodynamic information obtained for Ni−Mo_2C can be generalized to the Ni_2FeCo−Mo_2C system, phase diagram calculation software Pandat 2022 (*database source*: PanNi2022_TH+MB) was used to calculate the pseudo-binary phase diagrams for Ni−Mo_2C and Ni_2FeCo−Mo_2C, respectively (Figure S1). Ni and Ni_2FeCo both exhibit very limited solubility in Mo_2C, which further demonstrates the advantage of the carbothermal shock method in preparing supersaturated doped carbides. As schematically shown in Figure 1c, the structure derived from the nonequilibrium CTS has a homogeneous solid solution, where NiFeCo atoms are uniformly dispersed throughout the Mo_2C lattice to ensure maximized MSI and stabilization. However, the catalysts synthesized under near-equilibrium conditions via the furnace treatment, which is composed of phase-separated NiFeCo particles and less doped Mo_2C support, resulting in a heterogeneous structure, as denoted by H-Mo_2C, with limited MSI and stabilization.

As illustrated in Figure 1d, the doping of NiFeCo into the Mo_2C lattice at an optimal 20% content significantly boosts the OER activity and durability of the catalyst. This enhancement is attributed to the high dispersion of NiFeCo, which ensures a uniform distribution of active sites across the catalyst's surface. Furthermore, the synergistic effect between NiFeCo and Mo_2C optimizes the adsorption of reaction intermediates, leading to a more favorable catalytic activity.[36,37] Importantly, the high-density NiFeCo dopants within the Mo_2C lattice can dynamically restructure during the electrochemical OER process, forming a dense oxyhydroxide protective layer that shields the catalyst from degradation. Meanwhile, FeCoNi−Mo interactions can modify the electronic structure of the Mo_2C matrix and oxyhydroxide to have elevated dissolution potentials, which is crucial for the long-term stability of the catalyst. The above result indicates the importance of Max-MSI in metal carbide catalysts, where the synergistic effects between Ni_2FeCo and Mo_2C are maximized to significantly enhance the OER activity and durability.

The synthesis procedure for SD-Mo_2C is depicted in Figure 2a. A certain amount of precursor solution ($MoCl_5$, $NiCl_2$, $CoCl_2$, $FeCl_2$, molar ratio 16:2:1:1) was dropped onto the carbon paper, then dried, and subjected to CTS synthesis (~1200 °C, 600 ms) in an argon atmosphere, the temperature

https://doi.org/10.1021/acsnano.4c09249
ACS Nano XXXX, XXX, XXX−XXX

curve during CTS process is shown in Figure S2. During the high-temperature process of CTS, the precursor first generates Ni_2FeCo-doped MoO_2, where the oxygen source is mainly $MoOCl_3(EtOH)$ produced by alcoholysis, and rapidly reduces and carburizes to produce SD-Mo_2C. This synthesis process does not require additional carbon sources; the core carbon source comes from the carbon paper substrate. After the subsequent rapid cooling, the high-temperature structure is rapidly frozen, which keeps the structure of SD-Mo_2C. The crystal structure of the sample at different synthesis times was tested by X-ray diffraction (XRD). It can be observed that the sample existed in the form of Ni_2FeCo-MoO_2 at 200 ms, and the sample mainly changed into SD-Mo_2C with a small amount of MoO_2 residue at 400 ms. After the synthesis time was extended to 600 ms, SD-MoO_2 was completely transformed into SD-Mo_2C (Figure 2b). According to Gibbs free energy (Figure S3),[38,39] the tendency of Mo_2C generated by the reaction of MoO_2 with C is greater than that of Mo generated by the reaction of MoO_2 with C. Therefore, reduction and carburizing are carried out simultaneously in the process of CTS.

In contrast, the conventional furnace sintering method necessitates the addition of 2,5-dihydroxyterephthalic acid as a carbon source and requires a high temperature and long-time treatment (1000 °C, 6 h) to ensure the formation of Mo_2C.[40] XRD patterns of Mo_2C samples synthesized using both CTS and furnace treatment are presented in Figure S4. For the H-Mo_2C samples, the Ni peaks can be observed except for the peaks of orthorhombic Mo_2C, indicating the formation of metal on Mo_2C (i.e. H-Mo_2C). The incorporation of Ni_2FeCo atoms is expected to cause a reduction of unit cell parameters in the Mo_2C crystal due to their smaller atom radius compared to the Mo atoms in Mo_2C.

Further investigation about the influences of Ni_2FeCo ratios (Figure 2c, additional temperature curves during synthesis shown in Figure S5) uncovered that additional metal peaks occurred after Ni_2FeCo ratios exceeded 20%. Detailed XRD analysis of the (200) and (121) peaks for Ni_2FeCo ratios ranging from 0 to 30% revealed a significant shift toward higher angles for the doping ratios below 20%, suggesting a contraction of the unit cell as the doping content increased. However, for the ratios above 20%, the XRD angles remained scarcely changed, indicating that the lattice has reached its maximum doping capacity, and further increase of the Ni_2FeCo ratio no longer results in additional lattice contraction (Figure 2d). The cell parameters of SD-Mo_2C with different doping ratios are graphically represented (Figure 2e), which shows that 20% SD-Mo_2C has the lowest cell parameters. With the further addition of Ni_2FeCo, the cell parameters may have a certain increase, which may be due to the remaining Ni_2FeCo atoms being preferentially deposited on the second phase surface of the alloy, driven by the lattice fit.

The element contents of 20% SD-Mo_2C samples were further investigated by inductively coupled plasma optical emission spectrometry (ICP-OES), and the molar ratio of dopants in the 20% SD-Mo_2C samples was in Figure S6a, which is consistent with the intended doping ratio, demonstrating the excellent controlling ability of the CTS method for composition (Figure S6b). Moreover, a range of supersaturatedly doped transition-metal carbides can be generally synthesized by the CTS method. As shown in Figure 2f–h, for different Ni_2FeCo-doped carbides, only peaks of the corresponding carbides can be observed without the metal Ni peaks, indicating that the Ni_2FeCo-doped TiC, NbC, and W_2C samples were generally synthesized by the CTS method.[41,42] The three doped carbides all exhibit homogeneous structures without phase separation, which demonstrates the strong universality of our nonequilibrium synthesis method.

The nanoparticles with uniform particle size nanoparticles can be observed by transmission electron microscopy (TEM) (Figure 3a), which is beneficial for active site exposure, electrolyte immersion, and electron transfer, improving the catalytic performance. As shown in Figure 3b, a clear atomic lattice structure can be observed by high-resolution transmission electron microscopy (HR-TEM), and the *d*-spacing of the lattice is 0.212 nm, corresponding to the (200) crystal planes of the orthorhombic Mo_2C crystal. In H-Mo_2C samples, as shown in Figure 3c, larger particles with inconsistent shapes can be observed, which was caused by the extended sintering duration. Additionally, compared to the clean surface derived by the CTS method, using an organic carbon source results in carbon deposition, which hinders direct contact between the active site and the electrolyte, deteriorating the overall performance. As shown in Figure 3d, for H-Mo_2C samples, the *d*-spacing of the lattice is 0.218 nm. The energy-dispersive X-ray (EDX) spectroscopy mapping also confirms the elemental distribution. As shown in Figure 3e, the Mo, Ni, Co, Fe, and C elements in SD-Mo_2C are homogeneous and distributed across the samples, further indicating that doped Mo_2C samples were successfully synthesized. However, for the H-Mo_2C samples, the signal of the Ni element is separated from the samples (Figure 3f), indicating that Ni is precipitated from the Mo_2C, confirming less doping and heterostructures by conventional methods.

The elemental valence states and electronic structures of SD-Mo_2C and H-Mo_2C samples are also analyzed by X-ray photoelectron spectroscopy (XPS). By deconvoluting the Mo $3d_{5/2}$ peaks, we gained a deeper understanding of the electronic environment of Mo within these catalysts. As shown in Figure 3g, the Mo binding energy values of SD-Mo_2C samples were 228.43, 229.46, and 232.46 eV, for H-Mo_2C they were 228.71, 229.52, and 232.70 eV, and for pure Mo_2C, they were 229.5 and 231.2 eV, respectively. The Mo $3d_{5/2}$ peaks for SD-Mo_2C and H-Mo_2C were significantly shifted to lower binding energies compared to pure Mo_2C, proving that the addition of Ni_2FeCo significantly reduced the Fermi level of Mo.[43] Moreover, the peaks of SD-Mo_2C further shifted to lower binding energies compared to those of H-Mo_2C, indicating a stronger interaction between the Ni_2FeCo dopant and the Mo_2C support. The 2p XPS spectra of Ni, Fe, and Co in SD-Mo_2C and H-Mo_2C were further investigated as shown in Figure S7. The Ni $2p_{3/2}$ spectrum was deconvoluted into three distinct peaks at 853.1, 856.3, and 861.9 eV, corresponding to Ni^0, Ni–O, and satellite peaks. Similarly, the Co $2p_{3/2}$ spectrum exhibited four peaks at 778.4, 781.8, and 787.4 eV, indicating the presence of Co^0, Co–O, and satellite peaks. The Fe $2p_{3/2}$ spectrum was deconvoluted into four peaks at 707.7, 711.0, 714.5, and 717.8 eV, representing Fe^0, Fe–O species, and satellite peaks.[44] The valence distribution of the elements in each sample can be calculated by integrating the areas of the peaks after deconvolution. As illustrated in Figure 3h, the average valence states of Mo for SD-Mo_2C, H-Mo_2C, and pure Mo_2C were determined to be 2.38, 2.91, and 2.56, respectively. The proportion of Mo^0 of SD-Mo_2C (53%) is significantly higher than that of H-Mo_2C (38%) and pure Mo_2C (36%),

https://doi.org/10.1021/acsnano.4c09249
ACS Nano XXXX, XXX, XXX–XXX

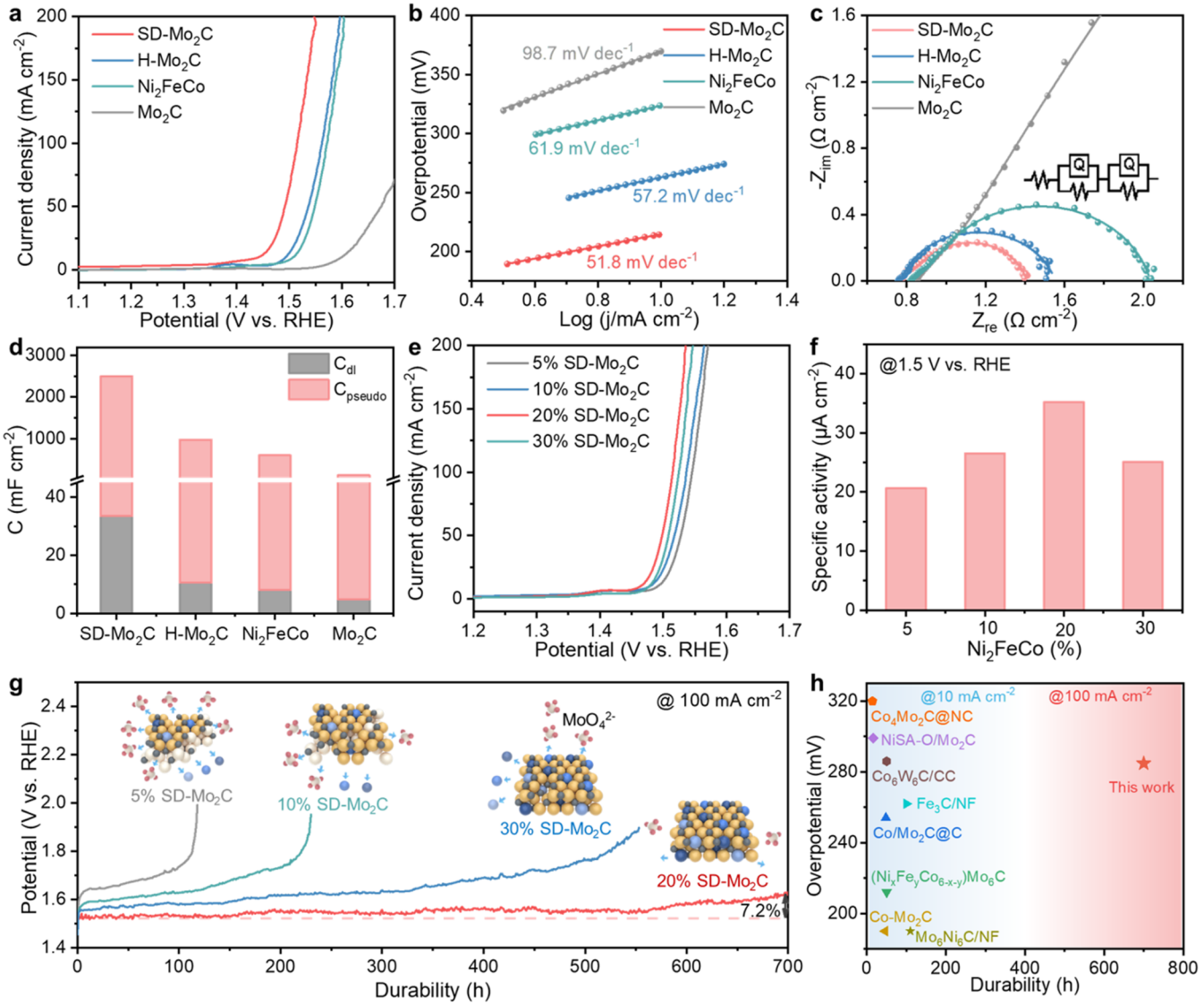

Figure 4. Electrochemical performance and analysis of various electrocatalysts in a 1 M KOH electrolyte. (a) LSV curves and (b) Tafel slope of different electrocatalysts. (c) Nyquist plots for different samples at 1.52 V; the inset shows the fitted circuit diagram. (d) Statistical comparison of C_{pseudo} and C_{dl} for the different catalysts. (e) LSV curves of different Ni_2FeCo ratios SD-Mo_2C. (f) ECSA-normalized activity for catalysts with different Ni_2FeCo ratios SD-Mo_2C at 1.50 V. (g) Stability of the OER at 100 mA cm^{-2} for materials with different Ni_2FeCo ratios, with schematic diagrams representing the dissolution trends of the various materials. (h) Activity and durability comparison of different carbide-based electrocatalysts.

indicating that more electron transfer from the Ni_2FeCo dopant to the Mo_2C host in SD-Mo_2C due to the higher incorporation of Ni_2FeCo into the Mo_2C lattice, and results in more metal−support interfaces.

Electrochemical OER Performance. The electrochemical OER performance of as-prepared samples was assessed by a typical three-electrode system in a 1 M KOH electrolyte. In order to prove the necessity of multielement doping, Ni_4−Mo_2C, Ni_3Fe−Mo_2C, Ni_2FeCo−Mo_2C, and NiFeCoMn−Mo_2C were prepared and tested by linear sweep voltamperes (LSV) (Figure S8a). The results show that multielement codoping can improve the catalytic activity better than single-element doping, and Ni_2FeCo−Mo_2C shows the best catalytic activity. Then, we prepared NiFe−Mo_2C, NiCo−Mo_2C, and FeCo−Mo_2C and verified the catalytic active sites, as shown in Figure S8b. The NiFe combination is considered the main source of catalytic activity, with Co as an additive that can further reduce the overpotential. Meanwhile, to optimize the ratio between Ni, Fe, and Co, samples with Ni:Fe:Co ratios of 1:1:1, 1:2:2, and 2:1:1 were prepared and subjected to LSV testing. The results showed that the sample with a ratio of 2:1:1 exhibited the best OER performance (Figure S8c).

To demonstrate the advantage of Ni_2FeCo doping in Mo_2C, compared to CTS-prepared SD-Mo_2C, furnace-prepared H-Mo_2C, CTS-prepared Ni_2FeCo alloy, and CTS-prepared pure Mo_2C samples, the SD-Mo_2C exhibited the best OER activity, as shown in Figure 4a, and the LSV curve without IR correction is shown in Figure S9. SD-Mo_2C exhibited a significantly lower overpotential of 214 mV at 10 mA cm^{-2} and 284 mV at 100 mA cm^{-2}, compared to that of H-Mo_2C (263 mV at 10 mA cm^{-2} and 332 mV at 100 mA cm^{-2}) and Ni_2FeCo (292 mV at 10 mA cm^{-2} and 358 mV at 100 mA cm^{-2}). Moreover, the Tafel slope value of SD-Mo_2C is 51.8 mV dec^{-1}, which is lower than that of H-Mo_2C (57.2 mV

https://doi.org/10.1021/acsnano.4c09249
ACS Nano XXXX, XXX, XXX−XXX

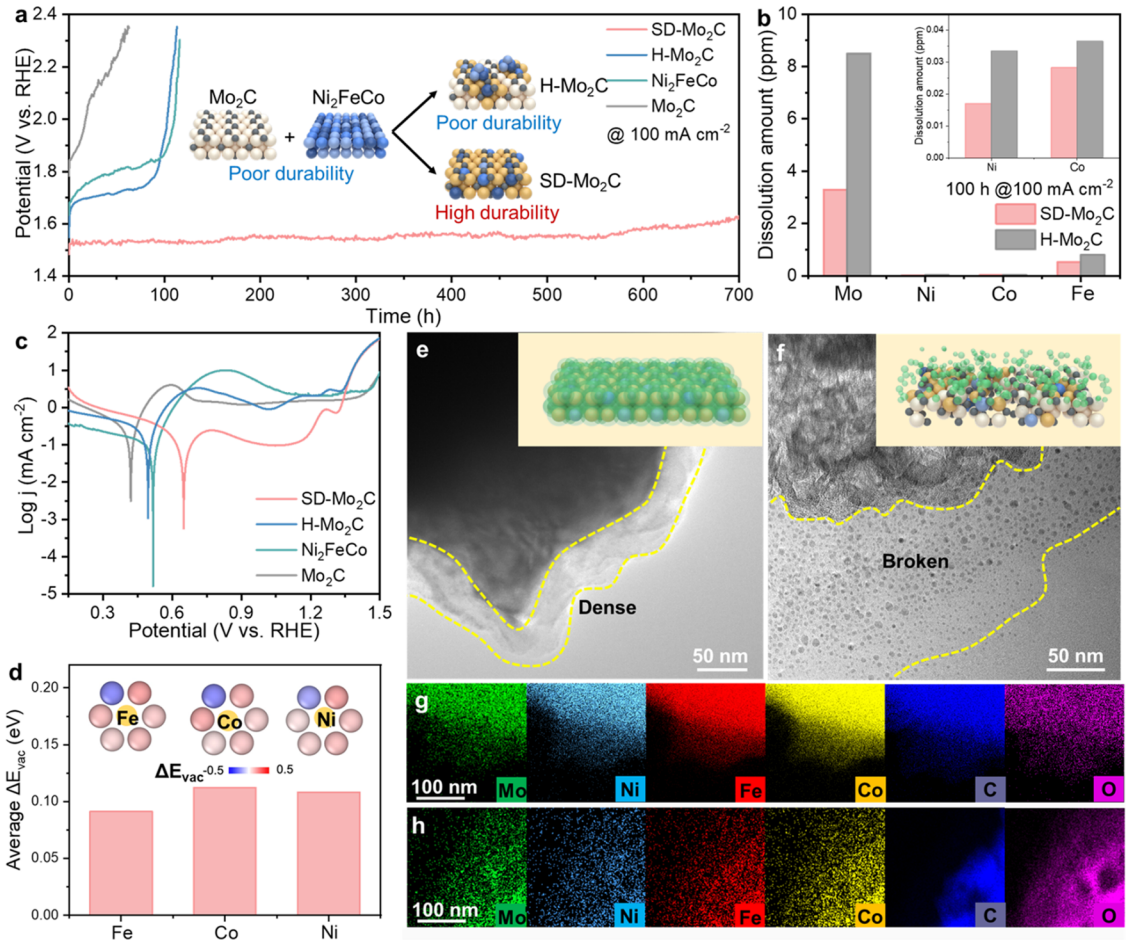

Figure 5. Stability analysis of various electrocatalysts. (a) Chronopotentiometry stability tests at 100 mA cm^{-2} for different catalysts in 1 M KOH. (b) Metal leaching rates of SD-Mo_2C and H-Mo_2C during the initial 100 h of stability measurement. (c) Polarization curves of SD-Mo_2C, H-Mo_2C, Ni_2FeCo, and Mo_2C. (d) Statistical diagram of the vacancy formation energy shift of Mo around different heteroatoms. Inset: vacancy formation energy of Mo around the heteroatom calculated. The red sphere indicates the increase of vacancy formation energy, and the blue sphere indicates the decrease of vacancy formation energy. (e–h) TEM morphology images and EDX mapping images of reconstructed SD-Mo_2C and H-Mo_2C.

dec^{-1}), Ni_2FeCo (61.9 mV dec^{-1}), and Mo_2C (127 mV dec^{-1}), indicating a faster intrinsic reaction kinetic rate for SD-Mo_2C samples (Figure 4b). The charge transfer efficiency of the catalysts was investigated by electrochemical impedance spectroscopy (EIS).[45] As shown in Figure 4c, the charge transfer resistance (R_{ct}) for SD-Mo_2C was significantly lower than that for H-Mo_2C and Ni_2FeCo, indicating a faster charge transfer rate for SD-Mo_2C samples. The electrochemical active surface area (ECSA) was determined by the double-layer capacitance (C_{dl}), as shown in Figure S10. The relatively high C_{dl} value observed for the SD-Mo_2C composite indicated an enhanced surface roughness.

The coverage of OH^- on the catalyst surface is an important factor in explaining the catalytic performance at high current density.[46] The adsorption quantity of the reactant species (OH^-) on the catalyst surface was investigated by pulsed voltammetry, which can directly measure the surface coverage by the reactant species via quantification of the total charge on the electrocatalyst surface (Figure S11). The relationship between the total charge accumulated (Q), current density (J), and the applied potential (E) was established in Figure S12.[47] The total charge capacitance (C_{total}) can be derived from the slope of the linear region in the Q-E plot. C_{total} is composed of pseudo-capacitance (C_{pseudo}) and C_{dl}, and the C_{pseudo} is obtained by OH^- adsorption. The C_{pseudo} values for SD-Mo_2C, H-Mo_2C, Ni_2FeCo, and Mo_2C are 2464.7, 817.8, 588.4, and 112.4 mF cm^{-2}, respectively (Figure 4d), suggesting a substantial coverage of the SD-Mo_2C catalyst surface by the reactant species, which is crucial for facilitating a robust OER process, especially at higher current densities.

To explore the influence of the MSI on the intrinsic catalytic activity of the electrocatalysts, linear sweep voltammetry (LSV) was performed on a range of SD-Mo_2C samples with varying Ni_2FeCo ratios from 5 to 30%, as shown in Figure 4e. The SD-Mo_2C samples with a 20% Ni_2FeCo ratio exhibited the most reactive among the tested materials, underscoring that the optimal doping (or Max-MSI) content is critical for improving the catalytic performance. As illustrated in Figures 4f and S13, the 20% SD-Mo_2C displayed a significant ECSA-normalized current density, indicating the 20% SD-Mo_2C with high intrinsic activity due to the Max-MSI between Ni_2FeCo with Mo_2C. EIS was utilized to further elucidate the kinetics of charge transfer during the OER. A comparison of the Nyquist plots, as presented in Figure S14, demonstrated that 20% SD-Mo_2C exhibited the smallest semicircle, indicating superior electronic conductivity and a more rapid charge transfer rate. The alignment between the C_{pseudo} on the catalyst surface and the normalized activity with increasing ratio substantiates that

https://doi.org/10.1021/acsnano.4c09249
ACS Nano XXXX, XXX, XXX−XXX

the material transport capacity on the catalyst surface is the principal determinant of catalytic activity at higher potentials (Figures S15−S17). These results highlight the importance of Max-MSI in tailoring the electronic structure and surface properties of the catalyst to optimize both the intrinsic reaction kinetics and the charge transfer processes.

The investigation into the impact of Max-MSI on the durability of SD-Mo_2C during the OER involved assessing samples with varying Ni_2FeCo ratios at a constant current density of 100 mA cm^{-2}. The results, as depicted in Figure 4g, show that the durability of 5−30% Ni_2FeCo feed ratio SD-Mo_2C is 100, 212, 700, and 484 h, respectively. For samples with 5 and 10% Ni_2FeCo doping, the doping levels were insufficient to affect all Mo sites within the Mo_2C structure. This incomplete interaction resulted in the partial dissolution of Mo_2C during the OER process. Conversely, when the Ni_2FeCo doping level exceeded 20%, excess Ni_2FeCo formed undoped Ni_2FeCo clusters that were less influenced by the Mo_2C support. These clusters were more prone to dissolution during the OER, leading to a destabilization of the catalyst. This observation highlights the importance of achieving the right balance in the doping levels to maintain the optimal Max-MSI and the stability of the catalyst. The SD-Mo_2C catalyst with 20% doping was found to achieve this optimal balance, offering the best synergistic effect between the support and active site. This optimal Max-MSI structure not only enhances the catalytic activity but also provides the necessary stability for long-term operation in OER applications. The findings underscore the significance of precise control over the doping process and the Max-MSI in the design of highly efficient and stable electrocatalysts for energy conversion technologies. Among the recent carbide-based materials, 20% SD-Mo_2C demonstrated comparable activity and durability toward the OER (Figure 4i). It should be noted that almost all reported carbide catalysts are tested at 10 mA cm^{-2}, while the durability test in this work was done at 100 mA cm^{-2}. Subsequently, to demonstrate the scalability of the preparation method, 20% SD-Mo_2C with three different areas of 4, 9, and 16 cm^2 were prepared (Figures S18 and S19a). All samples exhibited good OER performance by LSV testing (Figure S19b) and showed small particles and uniform morphology (Figure S19c). SD-Mo_2C can be prepared not only on carbon paper but also on metal substrates, such as nickel foam (NF), an additional carbon source is required. The XRD pattern of SD-Mo_2C/NF is shown in Figure S20a. Meanwhile, we tested the OER performance of SD-Mo_2C/NF, which also exhibited good OER activity and stability after 400 h at 100 mA cm^{-2} in 7 M KOH, and the potential only increased by 5.1% (Figure S20b,c), demonstrating the good durability of the material. Additionally, SEM and EDX characterizations showed that the SD-Mo_2C nanoparticles were evenly distributed and uniform in size on the NF surface (Figure S20d). This indicates that the thermal shock preparation method can be applied to a variety of substrate materials.

The stability of electrocatalysts is critical for their practical application as it directly determines the longevity and efficiency of energy conversion devices. In the study, we explored the origin of stability in SD-Mo_2C, and the durability of various SD-Mo_2C samples was tested. As illustrated in Figure 5a, the SD-Mo_2C catalyst demonstrated exceptional durability, which is significantly longer than that of the H-Mo_2C sample (75 h) and Ni_2FeCo, which, despite lasting for 95 h, experienced a notable increase in potential during the initial 25 h of operation. In contrast, the Mo_2C was directly dissolved during the OER process in 1 M KOH at a positive potential. These results showed that neither Ni_2FeCo nor Mo_2C had durability in an alkaline high-potential environment, and the simple heterostructural assembly of the two materials could not enhance durability with very limited MSI. In contrast, the Max-MSI effect obtained by supersaturated doping could stabilize Ni_2FeCo and Mo_2C mutually. Concurrently, CV aging experiments were used to simultaneously demonstrate the stability of 20% SD-Mo_2C. After 1000 cycles of CV scanning, the maximum current density decreased by only 7.6%, further proving the stability of the material (Figure S21).

The cation leaching from SD-Mo_2C and H-Mo_2C after 100 h of durability testing was investigated by ICP-OES measurements. As shown in Figure 5b, the dissolution amount of Mo, Ni, Co, and Fe in SD-Mo_2C was 3.29, 0.0171, 0.0282, and 0.526 ppm, significantly lower than the corresponding amount in H-Mo_2C (8.50, 0.0335, 0.0364, and 0.811 ppm), indicating that SD-Mo_2C experiences much slower elemental loss compared to H-Mo_2C. The corrosion resistance of the catalysts was further evaluated in 1 M KOH using polarization curves, as shown in Figure 5c. Compared to 0.491 V for H-Mo_2C, 0.518 V for Ni_2FeCo, and 0.421 V for Mo_2C, SD-Mo_2C exhibited a much higher dissolution potential of 0.651 V, indicating that SD-Mo_2C with greater thermodynamic stability is less prone to corrosion and degradation in the alkaline electrolyte. Additionally, the dissolution current of SD-Mo_2C is 0.197 mA cm^{-2}, which is lower than that of H-Mo_2C (0.292 mA cm^{-2}), and Mo_2C (0.284 mA cm^{-2}), further indicating that the SD-Mo_2C with enhanced kinetic stability is less likely to dissolve or corrode.

In order to investigate the origin of the enhanced stability of SD-Mo_2C, we conducted density functional theory (DFT) calculations to reveal how the introduction of Ni, Co, and Fe heteroatoms affects the stability of Mo_2C. We utilize a C-terminated β-Mo_2C (200) slab as our model, which has two distinct Mo sites on the surface: one coordinates with one surface C and two sublayer C (labeled as Mo), and one coordinates with two surface C and one sublayer C (Mo_2), as shown in Figure S22a. These findings indicate that Ni, Fe, and Co prefer to occupy the Mo_1 site, with respective formation energies (E_f) of −1.666 eV for Ni, −1.760 eV for Fe, and −1.759 eV for Co (as shown in Methods). This indicates the stable incorporation of these elements into the Mo_2C structure. Next, we examine how these heteroatoms affect the dissolution resistance of neighboring Mo atoms. The dissolution process initiates with a Mo atom detaching from the surface, creating a Mo vacancy, and the dissolution tendency is directly linked to the changes in the Mo vacancy formation energy when comparing undoped versus doped occasions.[48] Our calculations show that the presence of a heteroatom increases the average vacancy formation energy of six adjacent Mo atoms by 0.1082 eV for Ni, 0.0913 eV for Fe, and 0.1123 eV for Co, enhancing the overall stability by resisting Mo atom dissolution in Mo_2C (Figure 5d and Table S3). Although one of the six Mo sites shows a decrease in vacancy formation energy, potentially accounting for that Mo dissolution is still observable in the doped Mo_2C, the overall increase in dissolution resistance contributes to enhanced system stability.

Further investigation into the reconstruction process of SD-Mo_2C during the OER was conducted by examining the XRD

https://doi.org/10.1021/acsnano.4c09249
ACS Nano XXXX, XXX, XXX−XXX

patterns after 100 cycles of CV at varying potential ranges (Figure S23). A notable observation was the progressive decrease in the intensity of the Mo_2C peaks with the increase of potential. These peaks disappear entirely within the potential range of 1.55−1.70 V vs RHE. However, this disappearance does not imply the complete dissolution of SD-Mo_2C but is caused by water molecules infiltrating the Mo_2C lattice under high-potential alkaline conditions, and the formation of an amorphous hydrated molybdenum carbide species, denoted as $Mo_2C_x(H_2O)_y$.[49] In situ Raman spectroscopy, as depicted in Figure S24, supports the presence of oxyhydroxide on the surface of the catalysts under high alkaline potentials due to reconstruction.

Importantly, TEM images of the SD-Mo_2C and H-Mo_2C samples after the reconstruction process provide compelling evidence of the transformations, as shown in Figure 5e,5g. A dense layer of oxyhydroxide was observed at the edges of SD-Mo_2C. Such a complete encapsulation is a result of supersaturated doping of NiFeCo into Mo_2C with a high doping level, and their reconstruction to oxyhydroxide leads to such dense encapsulation. The dense encapsulation of oxyhydroxide can prevent the alkali solution from eroding $Mo_2C_x(H_2O)_y$, thereby enhancing the dynamic stability of the material. The EDX analysis of the post-reconstructed SD-Mo_2C catalyst confirms the continued presence of Mo within the material and a uniform distribution of Mo, Ni, Fe, Co, C, and O elements, indicating the core is composed of NiCoFe-doped $Mo_2C_x(H_2O)_y$ and the shell is composed mostly of NiCoFeMo oxyhydroxide. In contrast, the TEM images and EDX of the post-reconstructed H-Mo_2C sample show significant dissolution and permeable and broken surfaces with varying thicknesses (Figure 5f,5h). The presence of numerous small particles at the edge of the material is also observed, indicating that strong leaching occurred. This is because the doping level of NiFeCo in conventional H-Mo_2C by furnace heating is limited; thus, their reconstruction to oxyhydroxide can not build a sufficient encapsulation barrier to protect the vulnerable Mo_2C from serious dissolution, leading to a largely compromised stability for H-Mo_2C as compared to SD-Mo_2C. Finally, to verify the potential application of SD-Mo_2C in industrial water electrolysis, we tested the durability in a 7 M KOH solution. After being subjected to a current density of 100 mA cm^{-2} for 400 h, the potential of SD-Mo_2C increased by only 6.5%, demonstrating the excellent stability of SD-Mo_2C (Figure S25).

CONCLUSIONS

In conclusion, our research has successfully presented a typical synthesis approach for creating a supersaturated doping Mo_2C with Ni_2FeCo, alongside proposing a structural configuration that optimizes or maximizes the interaction between the metal and the support (i.e., Max-MSI). The Ni_2FeCo-Mo_2C with a Max-MSI structure can improve the activity and durability of the OER. Through meticulous control over the Ni_2FeCo doping levels, we have established the relationship between the degree of doping and the resulting catalytic performance and durability. Notably, the Mo_2C doped with 20% Ni_2FeCo stands out as the most effective catalyst, offering an overpotential of 284 mV at 100 mA cm^{-2}, and demonstrating the capability to operate stably at this current density for an impressive 700 h. Our findings underscore that a supersaturated doping level is essential for achieving the most beneficial interaction between the Ni_2FeCo active sites and the Mo support, thereby bolstering the overall efficacy. This study not only illuminates the potential of this high-performing OER catalyst but also provides an alternative approach for the design of advanced catalyst structures through a finely controlled MSI.

METHODS

Synthesis of 20% SD-Mo_2C. 0.2 M Ethanolic solutions of $MoCl_5$, $NiCl_2$, $CoCl_2$, and $FeCl_2$ were prepared. 400 μL of $MoCl_5$, 50 μL of $NiCl_2$, 25 μL of $CoCl_2$, and 25 μL of $FeCl_2$ solutions were mixed. Then, the mixture was dropped on a carbon paper cut to dimensions of 3 cm × 0.5 cm. The carbon paper was dried with a precursor at 105 °C. After drying, the carbon paper was CTS for 600 ms at 13A under the constant current mode in an argon atmosphere. The synthesis of other samples is similar to the above steps. Refer to the Supporting Information.

Material Characterizations. The diffraction parameter of the materials was characterized by the XRD diffractometer (XRD-7000, Shimadzu, Japan) with the Cu Kα radiation (λ = 0.15406 nm). The morphology and fine structure of the material were characterized by the TEM images. The HR-TEM images were obtained using a JEMARM300F2 microscope (JEOL, Ltd., Japan) at 300 kV. The elementary dispersity was measured by the ICP-OES instrument (720ES, Agilent). The binding energy of each element of the materials was analyzed by XPS (K-α, Thermo).

Electrochemical Measurements. The OER performance was tested in a three-electrode system at room temperature by an electrochemical station (CX310X, Corrtest, China), the Hg/HgO electrode and a graphite rod were used as the reference electrode and counter electrode, respectively. Twenty cycles of CV activation were applied from 1.12 to 1.62 V vs RHE at a scan rate of 100 mV s^{-1} before all electrochemical measurements in 1 M KOH. The scan rate of LSV was 2 mV s^{-1}, and the polarization curves were 90% IR-corrected.

ASSOCIATED CONTENT

Data Availability Statement

The data generated in this work are presented in this article and the Supporting Information, and are available from the corresponding authors upon request.

Supporting Information

The Supporting Information is available free of charge at https://pubs.acs.org/doi/10.1021/acsnano.4c09249.

Additional experimental procedures, additional characterization results (including SEM, XPS, and in situ Raman), additional electrochemical measurements (including LSVs, Tafel slopes, and pulse voltammetry protocol), DFT calculations, and temperature curves (PDF)

AUTHOR INFORMATION

Corresponding Authors

Yonggang Yao − *State Key Laboratory of Material Processing and Die & Mould Technology, School of Materials Science and Engineering, Huazhong University of Science and Technology, Wuhan 430074, China;* orcid.org/0000-0002-9191-2982; Email: yaoyg@hust.edu.cn

Bao Yu Xia − *Key Laboratory of Material Chemistry for Energy Conversion and Storage (Ministry of Education), School of Chemistry and Chemical Engineering, Huazhong University of Science and Technology, Wuhan 430074, China;* orcid.org/0000-0002-2054-908X; Email: byxia@hust.edu.cn

https://doi.org/10.1021/acsnano.4c09249
ACS Nano XXXX, XXX, XXX−XXX

Authors

Hanwen Liu − *State Key Laboratory of Material Processing and Die & Mould Technology, School of Materials Science and Engineering, Huazhong University of Science and Technology, Wuhan 430074, China*

Wenhui Shi − *State Key Laboratory of Material Processing and Die & Mould Technology, School of Materials Science and Engineering, Huazhong University of Science and Technology, Wuhan 430074, China*

Yaqing Guo − *State Key Laboratory of Material Processing and Die & Mould Technology, School of Materials Science and Engineering, Huazhong University of Science and Technology, Wuhan 430074, China; College of Chemistry and Materials Engineering, Wenzhou University, Wenzhou 325035, China*

Yunjie Mei − *State Key Laboratory of Material Processing and Die & Mould Technology, School of Materials Science and Engineering, Huazhong University of Science and Technology, Wuhan 430074, China*

Yi Rao − *State Key Laboratory of Material Processing and Die & Mould Technology, School of Materials Science and Engineering, Huazhong University of Science and Technology, Wuhan 430074, China*

Jinli Chen − *State Key Laboratory of Material Processing and Die & Mould Technology, School of Materials Science and Engineering, Huazhong University of Science and Technology, Wuhan 430074, China*

Shijing Liu − *State Key Laboratory of Material Processing and Die & Mould Technology, School of Materials Science and Engineering, Huazhong University of Science and Technology, Wuhan 430074, China*

Cheng Lin − *State Key Laboratory of Material Processing and Die & Mould Technology, School of Materials Science and Engineering, Huazhong University of Science and Technology, Wuhan 430074, China*

Anmin Nie − *Center for High Pressure Science, State Key Laboratory of Metastable Materials Science and Technology, Yanshan University, Qinhuangdao 066004, China*

Qi Wang − *Science and Technology on Surface Physics and Chemistry Laboratory, Mianyang 621908, China;* orcid.org/0000-0003-3418-8809

Yifei Yuan − *College of Chemistry and Materials Engineering, Wenzhou University, Wenzhou 325035, China;* orcid.org/0000-0002-2360-8794

Complete contact information is available at: https://pubs.acs.org/10.1021/acsnano.4c09249

Author Contributions

H.L. and W.S.: contributed equally to this work. H.L.: Investigation, methodology, writing & editing. W.S.: Writing—reviewing. Y.G.: Investigation. Y.M.: Investigation. Y.R.: Methodology. J.C.: Investigation. S.L.: Investigation. C.L.: Investigation. A.N.: Conceptualization, supervision, and editing. Q.W.: Investigation. Y.Yuan: Conceptualization, supervision, and editing. B.Y.X.: Supervision and editing. Y.Yao: Conceptualization, supervision, writing—reviewing and editing, funding acquisition.

Notes

The authors declare no competing financial interest.

ACKNOWLEDGMENTS

We acknowledge the National Key R&D Program of China (2021YFA1202300), the National Natural Science Foundation of China (Nos. 52401280, 52371223, 52101255), Shenzhen International Cooperation Program (GJHZ20220913143406013), the Open Fund of State Key Laboratory of New Textile Materials and Advanced Processing Technologies (FZ2022005), and the Interdisciplinary Research Program of Huazhong University of Science and Technology (2023JCYJ004). We thank test support from the Analytical and Testing Center of Huazhong University of Science & Technology and the State Key Laboratory of Materials Processing and Die & Mold Technology.

REFERENCES

(1) Chu, S.; Majumdar, A. Opportunities and challenges for a sustainable energy future. *Nature* **2012**, *488* (7411), 294−303.

(2) An, L.; Zhang, H.; Zhu, J.; Xi, S.; Huang, B.; Sun, M.; Peng, Y.; Xi, P.; Yan, C.-H. Balancing Activity and Stability in Spinel Cobalt Oxides through Geometrical Sites Occupation towards Efficient Electrocatalytic Oxygen Evolution. *Angew. Chem., Int. Ed.* **2023**, *62* (3), No. e202214600.

(3) Pan, S.; Li, H.; Liu, D.; Huang, R.; Pan, X.; Ren, D.; Li, J.; Shakouri, M.; Zhang, Q.; Wang, M.; Wei, C.; Mai, L.; Zhang, B.; Zhao, Y.; Wang, Z.; Graetzel, M.; Zhang, X. Efficient and stable noble-metal-free catalyst for acidic water oxidation. *Nat. Commun.* **2022**, *13* (1), No. 2294.

(4) Fan, Z.; Sun, Q.; Yang, H.; Zhu, W.; Liao, F.; Shao, Q.; Zhang, T.; Huang, H.; Cheng, T.; Liu, Y.; Shao, M.; Shao, M.; Kang, Z. Layered Quasi-Nevskite Metastable-Phase Cobalt Oxide Accelerates Alkaline Oxygen Evolution Reaction Kinetics. *ACS Nano* **2024**, *18* (6), 5029−5039.

(5) Zhang, N.; Hu, Y.; An, L.; Li, Q.; Yin, J.; Li, J.; Yang, R.; Lu, M.; Zhang, S.; Xi, P.; Yan, C.-H. Surface Activation and Ni-S Stabilization in NiO/NiS_2 for Efficient Oxygen Evolution Reaction. *Angew. Chem., Int. Ed.* **2022**, *61* (35), No. e202207217.

(6) Lee, W. H.; Han, M. H.; Ko, Y.-J.; Min, B. K.; Chae, K. H.; Oh, H.-S. Electrode reconstruction strategy for oxygen evolution reaction: maintaining Fe-CoOOH phase with intermediate-spin state during electrolysis. *Nat. Commun.* **2022**, *13* (1), No. 605.

(7) Cui, P.; Wang, T.; Zhang, X.; Wang, X.; Wu, H.; Wu, Y.; Ba, C.; Zeng, Y.; Liu, P.; Jiang, J. Rapid Formation of Epitaxial Oxygen Evolution Reaction Catalysts on Dendrites with High Catalytic Activity and Stability. *ACS Nano* **2023**, *17* (22), 22268−22276.

(8) Shi, W.; Liu, H.; Li, Z.; Li, C.; Zhou, J.; Yuan, Y.; Jiang, F.; Fu, K.; Yao, Y. High-entropy alloy stabilized and activated Pt clusters for highly efficient electrocatalysis. *SusMat* **2022**, *2* (2), 186−196.

(9) Zhong, H.; Zhang, Q.; Yu, J.; Zhang, X.; Wu, C.; Ma, Y.; An, H.; Wang, H.; Zhang, J.; Wang, X.; Xue, J. Fundamental Understanding of Structural Reconstruction Behaviors in Oxygen Evolution Reaction Electrocatalysts. *Adv. Energy Mater.* **2023**, *13* (31), No. 2301391.

(10) Yu, D.; Hao, Y.; Han, S.; Zhao, S.; Zhou, Q.; Kuo, C.-H.; Hu, F.; Li, L.; Chen, H.-Y.; Ren, J.; Peng, S. Ultrafast Combustion Synthesis of Robust and Efficient Electrocatalysts for High-Current-Density Water Oxidation. *ACS Nano* **2023**, *17* (2), 1701−1712.

(11) Xu, M.; Peng, M.; Tang, H.; Zhou, W.; Qiao, B.; Ma, D. Renaissance of Strong Metal-Support Interactions. *J. Am. Chem. Soc.* **2024**, *146* (4), 2290−2307.

(12) Ge, Y.; Qin, X.; Li, A.; Deng, Y.; Lin, L.; Zhang, M.; Yu, Q.; Li, S.; Peng, M.; Xu, Y.; Zhao, X.; Xu, M.; Zhou, W.; Yao, S.; Ma, D. Maximizing the Synergistic Effect of CoNi Catalyst on α-MoC for Robust Hydrogen Production. *J. Am. Chem. Soc.* **2021**, *143* (2), 628−633.

(13) Zhang, L.; Liu, H.; Song, B.; Gu, J.; Li, L.; Shi, W.; Li, G.; Zhong, S.; Liu, H.; Wang, X.; Fan, J.; Zhang, Z.; Wang, P.; Yao, Y.; Shi, Y.; Lu, J. Wood-inspired metamaterial catalyst for robust and

high-throughput water purification. *Nat. Commun.* **2024**, *15* (1), No. 2046.
(14) Kou, Z.; Yu, Y.; Liu, X.; Gao, X.; Zheng, L.; Zou, H.; Pang, Y.; Wang, Z.; Pan, Z.; He, J.; Pennycook, S. J.; Wang, J. Potential-Dependent Phase Transition and Mo-Enriched Surface Reconstruction of γ-CoOOH in a Heterostructured Co-Mo_2C Precatalyst Enable Water Oxidation. *ACS Catal.* **2020**, *10* (7), 4411−4419.
(15) Zhang, H.; Ouyang, Q.; Yu, L.; Hu, R.; Wan, J.; Song, B.; Huang, Q.; Yao, Y. Transient and in situ Growth of Nanostructured SiC on Carbon Fibers toward Highly Durable Catalysis. *Adv. Funct. Mater.* **2023**, *33* (32), No. 2301375.
(16) van Deelen, T. W.; Hernández Mejía, C.; de Jong, K. P. Control of metal-support interactions in heterogeneous catalysts to enhance activity and selectivity. *Nat. Catal.* **2019**, *2* (11), 955−970.
(17) Li, S.; Chen, B.; Wang, Y.; Ye, M.-Y.; van Aken, P. A.; Cheng, C.; Thomas, A. Oxygen-evolving catalytic atoms on metal carbides. *Nat. Mater.* **2021**, *20* (9), 1240−1247.
(18) Hou, M.; Zheng, L.; Zhao, D.; Tan, X.; Feng, W.; Fu, J.; Wei, T.; Cao, M.; Zhang, J.; Chen, C. Microenvironment reconstitution of highly active Ni single atoms on oxygen-incorporated Mo_2C for water splitting. *Nat. Commun.* **2024**, *15* (1), No. 1342.
(19) Chen, Y.; Liu, Y.; Zhai, W.; Liu, H.; Sakthivel, T.; Guo, S.; Dai, Z. Metastabilizing the Ruthenium Clusters by Interfacial Oxygen Vacancies for Boosted Water Splitting Electrocatalysis. *Adv. Energy Mater.* **2024**, *14*, No. 2400059.
(20) Hou, Z.; Cui, C.; Yang, Y.; Zhang, T. Electrochemical Oxidation Encapsulated Ru Clusters Enable Robust Durability for Efficient Oxygen Evolution. *Small* **2023**, *19* (29), No. 2207170.
(21) Wittke, J. P. Solubility of Iron in TiO_2 (Rutile). *J. Am. Ceram. Soc.* **1967**, *50* (11), 586−588.
(22) Fleischhammer, M.; Panthöfer, M.; Tremel, W. The solubility of Co in TiO_2 anatase and rutile and its effect on the magnetic properties. *J. Solid State Chem.* **2009**, *182* (4), 942−947.
(23) Jenisha, M. A.; Kavirajan, S.; Harish, S.; Archana, J.; Kamalabharathi, K.; Kumar, E. S.; Navaneethan, M. Interfacial engineering effect and bipolar conduction of Ni-doped MoS_2 nanostructures for thermoelectric application. *J. Alloys Compd.* **2022**, *895*, No. 162493.
(24) Zhao, L.; Bishop, S. R.; Hyodo, J.; Ishihara, T.; Sasaki, K. XRD and Raman Spectroscopy Study of Fe solubility in Cerium Oxide. *ECS Trans.* **2013**, *50* (40), 53.
(25) Weidow, J.; Johansson, S.; Andrén, H.-O.; Wahnström, G. Transition Metal Solubilities in WC in Cemented Carbide Materials. *J. Am. Ceram. Soc.* **2011**, *94* (2), 605−610.
(26) Miao, M.; Pan, J.; He, T.; Yan, Y.; Xia, B. Y.; Wang, X. Molybdenum Carbide-Based Electrocatalysts for Hydrogen Evolution Reaction. *Chem. - Eur. J.* **2017**, *23* (46), 10947−10961.
(27) Wei, J.; Tang, H.; Sheng, L.; Wang, R.; Fan, M.; Wan, J.; Wu, Y.; Zhang, Z.; Zhou, S.; Zeng, J. Site-specific metal-support interaction to switch the activity of Ir single atoms for oxygen evolution reaction. *Nat. Commun.* **2024**, *15* (1), No. 559.
(28) Feng, M.; Huang, J.; Peng, Y.; Huang, C.; Yue, X.; Huang, S. Tuning Electronic Structures of Transition Metal Carbides to Boost Oxygen Evolution Reactions in Acidic Medium. *ACS Nano* **2022**, *16* (9), 13834−13844.
(29) Shi, W.; Li, Z.; Gong, Z.; Liang, Z.; Liu, H.; Han, Y.-C.; Niu, H.; Song, B.; Chi, X.; Zhou, J.; Wang, H.; Xia, B. Y.; Yao, Y.; Tian, Z.-Q. Transient and general synthesis of high-density and ultrasmall nanoparticles on two-dimensional porous carbon via coordinated carbothermal shock. *Nat. Commun.* **2023**, *14* (1), No. 2294.
(30) Yao, Y.; Huang, Z.; Hughes, L. A.; Gao, J.; Li, T.; Morris, D.; Zeltmann, S. E.; Savitzky, B. H.; Ophus, C.; Finfrock, Y. Z.; Dong, Q.; Jiao, M.; Mao, Y.; Chi, M.; Zhang, P.; Li, J.; Minor, A. M.; Shahbazian-Yassar, R.; Hu, L. Extreme mixing in nanoscale transition metal alloys. *Matter* **2021**, *4* (7), 2340−2353.
(31) Yao, Y.; Dong, Q.; Brozena, A.; Luo, J.; Miao, J.; Chi, M.; Wang, C.; Kevrekidis, I. G.; Ren, Z. J.; Greeley, J.; Wang, G.; Anapolsky, A.; Hu, L. High-entropy nanoparticles: Synthesis-structure-property relationships and data-driven discovery. *Science* **2022**, *376* (6589), No. eabn3103.
(32) Yao, Y.; Huang, Z.; Xie, P.; Lacey, S. D.; Jacob, R. J.; Xie, H.; Chen, F.; Nie, A.; Pu, T.; Rehwoldt, M.; Yu, D.; Zachariah, M. R.; Wang, C.; Shahbazian-Yassar, R.; Li, J.; Hu, L. Carbothermal shock synthesis of high-entropy-alloy nanoparticles. *Science* **2018**, *359* (6383), 1489−1494.
(33) Liu, S.; Shen, Y.; Zhang, Y.; Cui, B.; Xi, S.; Zhang, J.; Xu, L.; Zhu, S.; Chen, Y.; Deng, Y.; Hu, W. Extreme Environmental Thermal Shock Induced Dislocation-Rich Pt Nanoparticles Boosting Hydrogen Evolution Reaction. *Adv. Mater.* **2022**, *34* (2), No. 2106973.
(34) Liu, Y.; Tian, X.; Han, Y.-C.; Chen, Y.; Hu, W. High-temperature shock synthesis of high-entropy-alloy nanoparticles for catalysis. *Chin. J. Catal.* **2023**, *48*, 66−89.
(35) Dmitrieva, G. P.; Razumova, N. A.; Shurin, A. K. Phase equilibria in alloys of the Ni-HfC-Mo2C system. *Soviet Powder Metall. Met. C* **1984**, *23* (9), 714−718.
(36) He, L.-G.; Cheng, P.-Y.; Cheng, C.-C.; Huang, C.-L.; Hsieh, C.-T.; Lu, S.-Y. (NixFeyCo6-x-y)Mo6C cuboids as outstanding bifunctional electrocatalysts for overall water splitting. *Appl. Catal., B* **2021**, *290*, No. 120049.
(37) Seh, Z. W.; Kibsgaard, J.; Dickens, C. F.; Chorkendorff, I.; Nørskov, J. K.; Jaramillo, T. F. Combining theory and experiment in electrocatalysis: Insights into materials design. *Science* **2017**, *355* (6321), No. eaad4998.
(38) Coltters, R. G. Thermodynamics of binary metallic carbides: A review. *Mater. Sci. Eng.* **1985**, *76*, 1−50.
(39) Gleiser, M.; Chipman, J. Free energy of formation of molybdenum oxide and carbide. *J. Phys. Chem. A* **1962**, *66* (8), 1539−1540.
(40) Zhang, L.; Hu, Z.; Huang, J.; Chen, Z.; Li, X.; Feng, Z.; Yang, H.; Huang, S.; Luo, R. Experimental and DFT studies of flower-like Ni-doped Mo_2C on carbon fiber paper: A highly efficient and robust HER electrocatalyst modulated by $Ni(NO_3)_2$ concentration. *J. Adv. Ceram.* **2022**, *11* (8), 1294−1306.
(41) Deng, B.; Wang, Z.; Chen, W.; Li, J. T.; Luong, D. X.; Carter, R. A.; Gao, G.; Yakobson, B. I.; Zhao, Y.; Tour, J. M. Phase controlled synthesis of transition metal carbide nanocrystals by ultrafast flash Joule heating. *Nat. Commun.* **2022**, *13* (1), No. 262.
(42) Han, Y.-C.; Liu, M.-L.; Sun, L.; Li, S.; Li, G.; Song, W.-S.; Wang, Y.-J.; Nan, Z.-A.; Ding, S.-Y.; Liao, H.-G.; Yao, Y.; Stucky, G. D.; Fan, F. R.; Tian, Z.-Q. A general method for rapid synthesis of refractory carbides by low-pressure carbothermal shock reduction. *Proc. Natl. Acad. Sci. U.S.A.* **2022**, *119* (37), No. e2121848119.
(43) Thornton, J. M. C.; Williams, R. H. A photoemission study of passivated silicon surfaces produced by etching in solutions of HF. *Semicond. Sci. Technol.* **1989**, *4* (10), 847.
(44) NIST X-ray Photoelectron Spectroscopy Database, NIST Standard Reference Database Number 20; National Institute of Standards and Technology: Gaithersburg, MD, 20899, 2000.
(45) Martirez, J. M. P.; Carter, E. A. Unraveling Oxygen Evolution on Iron-Doped β-Nickel Oxyhydroxide: The Key Role of Highly Active Molecular-like Sites. *J. Am. Chem. Soc.* **2019**, *141* (1), 693−705.
(46) Guo, H.; Yang, Y.; Yang, G.; Cao, X.; Yan, N.; Li, Z.; Chen, E.; Tang, L.; Peng, M.; Shi, L.; Xie, S.; Tao, H.; Xu, C.; Zhu, Y.; Fu, X.; Pan, Y.; Chen, N.; Lin, J.; Tu, X.; Shao, Z.; Sun, Y. Ex Situ Reconstruction-Shaped Ir/CoO/Perovskite Heterojunction for Boosted Water Oxidation Reaction. *ACS Catal.* **2023**, *13* (7), 5007−5019.
(47) Shen, W.; Zheng, Y.; Hu, Y.; Jin, J.; Hou, Y.; Zhang, N.; An, L.; Xi, P.; Yan, C.-H. Rare-Earth-Modified NiS_2 Improves OH Coverage for an Industrial Alkaline Water Electrolyzer. *J. Am. Chem. Soc.* **2024**, *146* (8), 5324−5332.
(48) Shi, F.; Gao, W.; Shan, H.; Li, F.; Xiong, Y.; Peng, J.; Xiang, Q.; Chen, W.; Tao, P.; Song, C.; Shang, W.; Deng, T.; Zhu, H.; Zhang, H.; Yang, D.; Pan, X.; Wu, J. Strain-Induced Corrosion Kinetics at Nanoscale Are Revealed in Liquid: Enabling Control of Corrosion Dynamics of Electrocatalysis. *Chem* **2020**, *6* (9), 2257−2271.

https://doi.org/10.1021/acsnano.4c09249
ACS Nano XXXX, XXX, XXX−XXX

(49) Maslennikov, A.; Cannes, C.; Fourest, B.; Boudanova, N.; Vivier, V.; Moisy, P. Dissolution and electrochemical properties of molybdenum carbide (Mo2C) in basic solutions. *Radiochim. Acta* **2007**, *95* (7), 399−408.

https://doi.org/10.1021/acsnano.4c09249
ACS Nano XXXX, XXX, XXX−XXX